https://doi.org/10.5194/egusphere-2026-765
Preprint. Discussion started: 11 March 2026
© Author(s) 2026. CC BY 4.0 License.

Raman lidar-derived aerosol optical properties and classification during the FENNEC experiment – Coherence with CAMS data

Patrick Chazette

LSCE/IPSL, CNRS-CEA-UVSQ, University Paris-Saclay, CEA Saclay, 91191 Gif sur Yvette, France

Correspondence to: Patrick Chazette (patrick.chazette@lsce.ipsl.fr)

Abstract. As part of the FENNEC programme, a field campaign was conducted on the Mediterranean coast of southern Spain, close to Gibraltar, from June to August 2011. Using a relatively straightforward ground-based N_2–Raman lidar, several aerosol optical properties were retrieved at 355 nm, including the linear particle depolarisation ratio (PDR), the lidar ratio (LR), and the aerosol backscatter and extinction coefficients. Of the 58 sampled nights, several periods were identified in which aerosol events exhibited optical thicknesses greater than 0.5. The primary causative agents of these events are the influx of Saharan dust mixed with local polluted and marine air masses. Pairing PDR and LR has been shown to be significant in identifying three distinct bulk aerosol classes: dust, carbonaceous and soluble (predominantly marine) aerosols. After processing the night-time data to ensure sufficient lidar range, the study demonstrates the efficiency of lidar profiles in evaluating the reliability of the Copernicus Atmosphere Monitoring Service (CAMS) reanalyses of atmospheric aerosols up to approximately 7 km above mean sea level (a.m.s.l.). The two datasets show excellent consistency in terms of the optical thickness and vertical profile of the aerosol extinction coefficient in the Saharan dust aerosol layers. CAMS reproduces the temporal evolution well, with a correlation coefficient (COR) greater than 0.8. However, this is less true for the layer below 2 km a.m.s.l. (COR = 0.56), where there is a tendency for CAMS to underestimate compared to ground-based lidar.

Keywords: FENNEC, aerosols, Raman, Lidar, CAMS, Mediterranean, Spain

1 Introduction

The Mediterranean region has been identified as one of the “hotspots” in projections of future climate change (Giorgi and Lionello, 2008), a worrying trend which will have far-reaching consequences for the region and the rest of the world (IPCC, 2022). All climate models show the Mediterranean basin drying up, particularly in the west. An increase in average temperature

https://doi.org/10.5194/egusphere-2026-765
Preprint. Discussion started: 11 March 2026
© Author(s) 2026. CC BY 4.0 License.

of around 4.5°C is projected by the end of the 21st century. This is associated with a drastic decline in rainfall of almost 30% compared with levels in the 2000s, along with a drop in available freshwater resources (IPCC, 2022). The Mediterranean coast's complex topography is chief among the causes, leading to contrasting air mass circulations in the lower and middle troposphere (Rodríguez et al., 2001). These air masses are known to transport various types of aerosols, whose physicochemical and optical properties are closely linked to their sources (Gallero et al., 2006). Consequently, these aerosols play a significant role in the surface radiation balance and, in turn, the regional meteorology and climate.

The aerosol impact on sea surface temperature, evaporation and precipitation has already been estimated using mesoscale models (e.g. Nabat et al., 2015). However, the variability of aerosols within the atmospheric column and over time has not yet been sufficiently considered in these models. In general, the concentrations and chemical composition of aerosols vary considerably depending on the season. These variations could induce local radiative forcings that would greatly offset the effects of greenhouse gases (Ghan, 2013; Bellouin et al., 2020), and the associated uncertainties are of comparable magnitude to the effects themselves (Forster et al., 2007). Therefore, the representation of the direct and semi-direct effects of aerosols in models is still insufficient. Furthermore, depending on their chemical composition, aerosols act as condensation or ice-forming nuclei, thereby modifying the radiative properties and lifetime of clouds (Kaufman et al., 2002), therefore the radiative budget of the Earth system. Current studies investigate the intensity of the aerosol impacts on precipitation. It is worth noting that recent work has shown that the radiative effect of dust aerosols has little impact on the amount or location of rainfall in the Western Mediterranean basin (Flamant et al., 2015). Significant improvements could be made by assimilating lidar profiles directly into short-term forecast models dedicated to air quality or meteorological applications (Wang et al., 2013, 2014a; Benedetti et al., 2009; Huneeus et al., 2012; Fourrié et al., 2019), in which lidar vertical profiles could play a pivotal role.

During the extended summer period from mid-June to the end of August 2011, the vertical distribution of aerosols was examined by installing a ground-based remote sensing station in San Pedro Alcantara, a municipality in southern Spain, situated between Gibraltar and Marbella, in Andalusia (36°29'11" N, 4°59'33" W). This installation formed part of the FENNEC programme, which took place from June to July 2011 (Ryder et al., 2015). The FENNEC experiment, which collected a large lidar dataset took place over a decade before the Mediterranean dust experiment (MEDUSE) (Hamonou et al., 1999; Dulac and Chazette, 2003)

https://doi.org/10.5194/egusphere-2026-765
Preprint. Discussion started: 11 March 2026
© Author(s) 2026. CC BY 4.0 License.

and preceding the Chemistry and Aerosol in the Mediterranean Experiment (ChArMEx), between 2013 and 2014 (Chazette et al., 2016b; Di Girolamo et al., 2020; Chazette et al., 2019; Mallet et al., 2015). During the same period, the European Aerosol Research Lidar Network (EARLINET) supplemented the ChArMEx observations, focusing primarily on aerosols of desert origin (Barragan et al., 2017). In parallel, a statistical study of the optical properties of aerosols obtained from Raman lidar profiles was conducted at the EARLINET station in Granada between 2008 and 2010 (Navas-Guzmán et al., 2013). This work revealed significant variability in aerosol properties over the study period.

This article examines the evolution of aerosol optical properties in the troposphere over time during the FENNEC ground-based field campaign, focusing on identifying the types of aerosols (e.g. dust, carbonaceous and soluble) using a relatively straightforward N_2–Raman lidar. The optical apportionment of the aerosols is then compared with the mesoscale modelling of the aerosol's chemical composition, as provided by the Copernicus Atmosphere Monitoring Service (CAMS; https://atmosphere.copernicus.eu/, last access: 8 February 2026). Section 2 describes the experimental site and the primary tools employed. Section 3 outlines the method for inverting lidar data and retrieve the aerosol extinction coefficient from CAMS products. Section 4 presents and discusses the vertical profiles of the retrieved aerosol optical properties, alongside the lidar-derived aerosol speciation. Section 5 discusses consistency with CAMS simulations. Section 6 concludes.

2 Experimental set up and tools

2.1 Ground-based observations

2.1.1 Description

A temporary ground-based station was installed in San Pedro Alcantara, Andalusia, in the summer of 2011 (Figure 1a). This enabled continuous optical measurements within the atmospheric column from 25 June to 2 August 2011. The seaside location was chosen due to the potential for i) strong events of particle transport from the Sahara, ii) presence of pollution or biomass fire plumes, and iii) high variability in aerosol optical thickness (AOT) (Rodríguez et al., 2001; Toledano et al., 2007). Located at an altitude of 110 m above mean sea level (a.m.s.l.), the station offered a 360° panoramic view.

https://doi.org/10.5194/egusphere-2026-765
Preprint. Discussion started: 11 March 2026
© Author(s) 2026. CC BY 4.0 License.

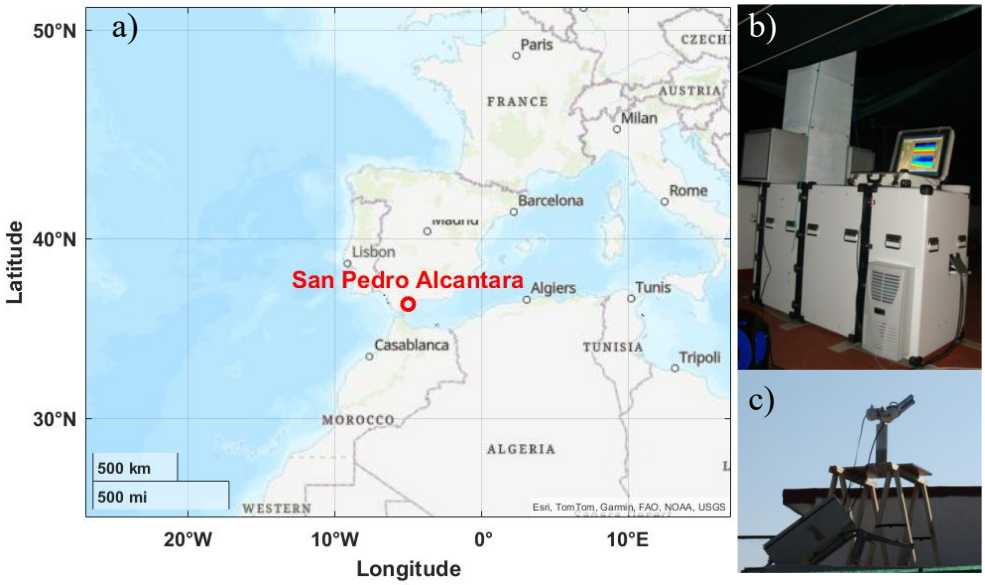

Figure 1. a) Location of the ground-based station (in red) where b) the LAASURS lidar and c) the sun photometer were installed.

2.1.2 Ground-based Raman lidar

LAASURS (Lidar for Automatic Atmospheric Surveys using Raman Scattering) is the precursor to the Water vapour and Aerosol LIdar (WALI), which was used in a series of Mediterranean experiments (Chazette et al., 2016a, 2014). LAASURS (Figure 1b) itself is described in detail and validated in Royer et al. (2011a) and Chazette et al. (2019b). The main characteristics of LAASURS are given in Table 1. Its wide field-of-view (FOV) of ~2.3 mrad enables full overlap of the transmission and reception paths at distances of ~200 metres. Three different channels record the total elastic backscatter signal of the atmosphere (elastic channels), the cross-polarised elastic backscatter signal of the atmosphere with respect to the laser emission, and the inelastic nitrogen vibrational Raman backscattered signal (N_2–Raman channel). Using the N_2–Raman channel at night allows the total AOT and the cumulative AOT profiles to be retrieved. When this is combined with the elastic channel, the lidar ratio (LR) is derived (Royer et al., 2011a).

The lidar measured atmospheric properties with a temporal native resolution of approximately 50 s, i.e. an average of 1,000 elementary profiles, and a vertical resolution of 0.75 m. In order to pass through desert aerosol layers, which can reach heights of over 7 km, it is necessary to reduce the temporal and vertical resolutions. The profiles are averaged over nights and the vertical resolution is reduced to 100 metres to improve the signal-to-noise ratio (SNR) and enable access to the upper troposphere (see Section 3).

https://doi.org/10.5194/egusphere-2026-765
Preprint. Discussion started: 11 March 2026
© Author(s) 2026. CC BY 4.0 License.

Table 1. Main characteristics of LAASURS.

Reception channels	Elastic // (354.67 nm) Elastic ⊥ (354.67 nm) N_2–Raman (387 nm)
Pulse repetition rate	20 Hz
Emitted energy	16 mJ
Pulse duration	7-8 ns
Beam diameter	25 mm
Divergence	< 0.2 mrad
Reception diameter	150 mm
Filter bandwidth	Elastic: 0.3 nm N_2–Raman: 0.2 nm
Field of view	2 × 0.67 mrad
Detector	Photomultiplier
Detection mode	Day: Analogue Night: Analogue/photon counting
Digitalization	12 bits
Native/final line of sight resolution	0.75 m/100 m

2.1.3 Sun photometer

A sun photometer (Figure 1c) was installed at the temporary lidar site during the experiment to provide supplementary measurements to complement those obtained by lidar. In this study, both ultraviolet and visible optical thicknesses are taken into consideration. These are then combined with the Angstrom coefficient, calculated between 380 and 500 nm, in order to determine the AOT at 355 nm during daytime. Sun photometer data are derived from the AErosol RObotic NETwork (AERONET) temporary stations in San Pedro Alcantara (http://aeronet.gsfc.nasa.gov/, last access: 24 January 2026). Level 2 data, which has undergone cloud screening (Dubovik and King, 2000), are used. The AOT is retrieved with a maximum absolute uncertainty of 0.02, independent of the aerosol load.

2.2 CAMS

CAMS global reanalysis (EAC4) has a horizontal resolution of 0.75° × 0.75° and is provided by the Copernicus Atmosphere Monitoring Service (CAMS, https://atmosphere.copernicus.eu/, last access: 24 January 2026) (Inness et al., 2019). This study analyses the consistency of EAC4 with the optical apportionment of aerosols derived from LAASUR's vertical profiles. CAMS combines model data with various observations from across the world. In particular, AOTs derived from satellite observations, such as those of the Moderate Resolution Imaging Spectroradiometer (MODIS) (Remer et al., 2005), are directly assimilated into the model, as are ground-based measurements from permanent AERONET stations. However, vertical aerosol profiles are not assimilated. CAMS provides data on aerosol compounds: desert dust, sea salt, organic matter, black carbon, sulphate ions. In the following, soot and organic carbons

https://doi.org/10.5194/egusphere-2026-765
Preprint. Discussion started: 11 March 2026
© Author(s) 2026. CC BY 4.0 License.

are grouped together as "carbonaceous" aerosols, while ionic concentrations and sea salt are grouped together as "soluble". It should be noted that the primary source of the latter aerosol types is marine for the site under consideration. As indicated by the findings of the research, dust, when present above the lidar station, serves as an indicator of the transport of Saharan aerosols. Carbonaceous aerosols, meanwhile, serve as an indicator of combustion (e.g. from traffic, industry, and forest fires). Finally, soluble aerosols serve mainly as an indicator of marine origins.

3 Method

3.1 Lidar-derived aerosol optical properties

During daylight hours, the range of the lidar is insufficient to determine the aerosol extinction coefficient (AEC), lidar ratio (LR) and linear particle depolarisation ratio (PDR) simultaneously. In order to ascertain the nature of the aerosols, i.e. whether they are dust-like, sea salt or polluted aerosols, it is necessary to evaluate these three optical parameters (Chazette et al., 2016a). This means collecting data at night and averaging it over a six-hour period, between 11 p.m. the previous day and 5 a.m. the following day. The SNR (SNR $\gtrsim$ 10) is sufficient for inverting mean lidar profiles up to 8 km a.m.s.l., with an altitude zone between 7 and 8 km a.m.s.l. in which molecular scattering accounts for over 99% of the total extinction. The mean lidar profiles thus exhibit a molecular slope between 7 and 8 km a.m.s.l., as illustrated in Figure 2. The procedure used to invert the lidar profiles considers all LAASURS channels.

The range-corrected elastic lidar signal S_E is expressed as a function of altitude z (e.g. Measures, 1984; Ansmann et al., 1992)

$$S_E(z) = C_E \cdot \left(\beta_m(z) + \beta_a(z)\right) \cdot F_E(z) \cdot exp\left[-2 \cdot \left(MOT(z) + AOT(z)\right)\right] \quad (1)$$

The instrumental constant C_E of the elastic channel is independent of altitude, while the overlap function F_E tends towards 1 from 200 m (Royer et al., 2011b). The molecular (β_m) and particular (β_a) backscatter coefficients are provided for an emitted wavelength of 354.67 nm. The atmospheric attenuation is characterised by the molecular (MOT) and the AOT.

For the N_2–Raman channel, the range-corrected lidar signal is given by (e.g. Royer et al., 2011a)

$$S_R(z) = C_R \cdot F_R(z) \cdot N_m(z) \cdot exp[-(1+\eta_m) \cdot MOT(z) - (1+\eta_a) \cdot AOT(z)] \quad (2)$$

with

https://doi.org/10.5194/egusphere-2026-765
Preprint. Discussion started: 11 March 2026
© Author(s) 2026. CC BY 4.0 License.

$$\eta_m = \left(\frac{387}{354.67}\right)^{-4.09}$$
$$\eta_a = \left(\frac{387}{354.67}\right)^{-A} \quad (3)$$

The instrumental constant of the inelastic channel system is C_R, and the overlap function is F_R. In this equation, the Ångström exponent A must be considered. Here, A has been derived from the interpolation of the sun photometer measurements (Figure 3). By normalising Equation 3 to a reference altitude z_0 located at the bottom of the profile, where the overlap functions are well-defined (for example, when it tends towards 1), the AOT between z_0 and z can be expressed as follows:

$$AOT(z_0, z) = \frac{1}{1+\eta_a} \cdot \left[\log\left(\frac{N_m(z)}{N_m(z_0)} \cdot \frac{S_R(z_0)}{S_R(z)}\right) - (1+\eta_m) \cdot MOT(z_0, z)\right] \quad (4)$$

This assumes a constant spectral variation of aerosol optical properties with altitude. The molecular contribution is calculated using the Nicolet (1984) model. The ERA5 reanalyses (Hersbach et al., 2020) from the European Centre for Medium-Range Weather Forecasts (ECMWF) are used as input data. These have been given for the geographical location of the lidar. The AEC (α_a) can then be calculated using a derivative low-pass filter of AOT with respect to z, as described by Dieudonné et al. (2015):

$$\alpha_a(z_0, z) = \frac{\partial AOT(z_0, z)}{\partial z} \quad (5)$$

For SNRs greater than 10, the margin of error is between 0.01 and 0.02 km^{-1}, which is larger at higher altitudes.

In Equation 1, the atmospheric transmission must be corrected in order to calculate β_a. In order to maintain the correction at second order in terms of uncertainty, it is preferable to consider the ratio between the elastic and inelastic channels. In the molecular zone between 7 and 8 km a.m.s.l., this ratio can be evaluated using the relationship:

$$\frac{C_E}{C_R} = \langle \frac{S_E(z)}{S_R(z)} \cdot exp[(1-\eta_m) \cdot MOT(z)] \rangle_{mol} \quad (6)$$

This method has been demonstrated to be efficient for calibrating lidar measurements in clear-sky conditions. The calculation is performed by averaging over the molecular altitude range ($\langle \quad \rangle_{mol}$). For all altitudes z, β_a is then given by the same channel ratio:

https://doi.org/10.5194/egusphere-2026-765
Preprint. Discussion started: 11 March 2026
© Author(s) 2026. CC BY 4.0 License.

$$\beta_a(z) = \left(\frac{C_R}{C_E} \cdot \frac{S_E(z)}{S_R(z)} \cdot exp[(1-\eta_m) \cdot MOT(z)] \cdot exp[(1-\eta_a) \cdot AOT(z)] - 1\right) \cdot \beta_m(z) \quad (7)$$

The extinction-to-backscatter ratio (Lidar Ratio, LR) is subsequently determined by the following formula, which is dependent upon altitude:

$$LR(z) = \frac{\alpha_a(z)}{\beta_a(z)} \quad (8)$$

Royer et al. (2011a) used a Monte Carlo approach founded upon a Tikhonov regularisation method (Tikhonov and Arsenin, 1978) to demonstrate that the relative errors on LR were 3% and 8% for AOTs of 0.1 and 0.5, respectively.

The final optical parameter to be deduced is the PDR, which is expressed as follows (Chazette et al., 2012) :

$$PDR(z) = \frac{\beta_m(z) \cdot \left(VDR_m - VDR(z)\right) - \beta_a(z) \cdot VDR(z) \cdot (1 + VDR_m)}{\beta_m(z) \cdot (VDR(z) - VDR_m) - \beta_a(z) \cdot (1 + VDR_m)} \quad (9)$$

In accordance with Collis and Russel (1976), the molecular volume depolarization ratio (VDR_m) is taken to be 0.3945% at 355 nm. The VDR is calculated according to the method described by Chazette et al. (2012). The PDR absolute uncertainties range from 1 to 2% for the encountered AOTs at 355 nm (AOT > 0.2) (Dieudonné et al., 2017).

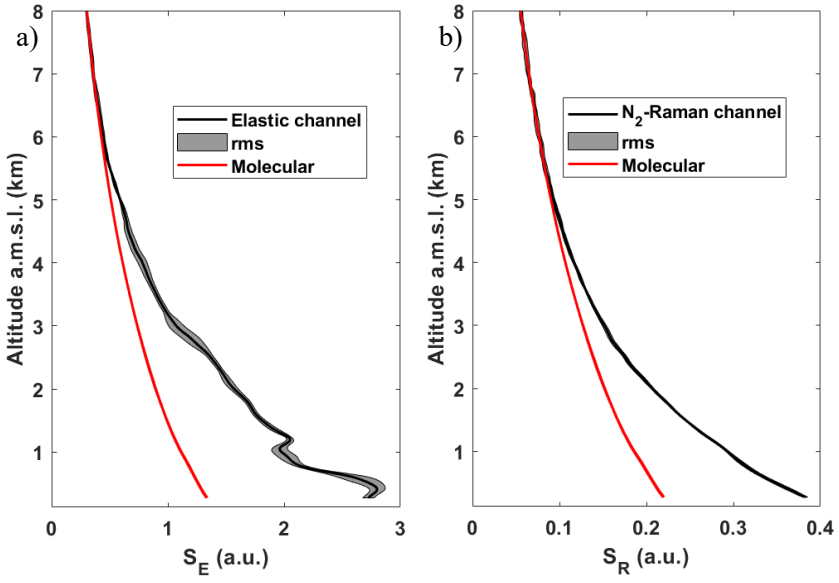

https://doi.org/10.5194/egusphere-2026-765
Preprint. Discussion started: 11 March 2026
© Author(s) 2026. CC BY 4.0 License.

Figure 2. The mean vertical profiles of the range-corrected a) elastic (S_E) and b) Raman (S_R) channels are shown for the night of 27-28 June 2011, from 23:00 to 05:00. The grey area shows the standard deviation of the mean vertical profiles. The red solid line indicates the molecular contribution.

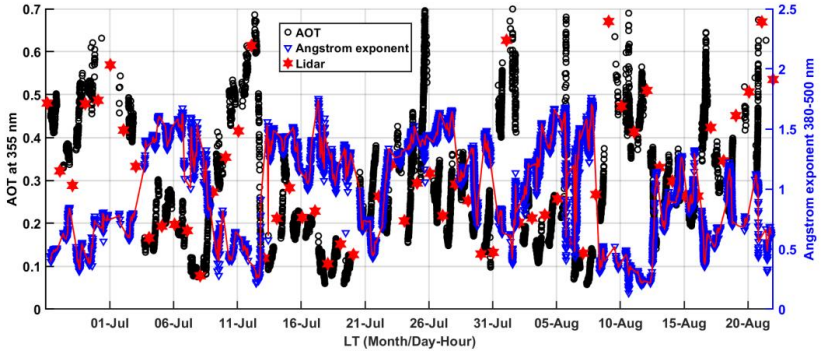

Figure 3. Temporal evolution of the sun photometer-derived aerosol optical thickness (AOT) at 355 nm and the Ångström exponent between 380 and 500 nm. The red solid line shows the interpolation used for the lidar profile inversion at night. The red star shows the lidar-derived AOT at night, from 23:00 to 05:00 local time (LT).

3.2 CAMS-derived Aerosol optical properties

CAMS products contain AOTs for the different classes of aerosol compound. These AOTs are provided at different wavelengths. The wavelengths closest to the lidar wavelength are used, i.e. 469 and 550 nm. This allows the Ångström exponent (A) predicted by the model to be derived. It is then used to convert the AOT at 550 nm (AOT_{550}) to the AOT at 355 nm (AOT_{355}) using the relationship (Ångström, 1964):

$$AOT_{355} = AOT_{550} \cdot \left(\frac{355}{550}\right)^{-A} \quad (10)$$

However, AEC profiles (α_{CAMS}) are not given directly. They can be evaluated using the mixture ratios r_i of each compound i (i.e. dust, carbonaceous and soluble) provided by CAMS with AOTs at 550 nm as a constraint. They are expressed according to the relationship:

$$\alpha_{CAMS}(z) = \frac{M_a}{\mathcal{N}} \cdot n_a(z) \cdot \sum_{i=1}^{3} r_i(z) \cdot \sigma_{spec,i} \quad (11)$$

where M_a is the molar mass of dry air (28.94 g), $\mathcal{N}$ is Avogadro's number (6.022 10^{23}) and n_a is the atmospheric density. The specific cross sections $\sigma_{spec,i}$ at 550 nm are calculated by adjusting the AOTs for each compound. The values thus determined are shown in Table 2.

The matching between the AOTs provided by CAMS and those recalculated from the AEC profiles in Eq. 11 is evaluated using statistical parameters defined in Appendix A. Their values

https://doi.org/10.5194/egusphere-2026-765
Preprint. Discussion started: 11 March 2026
© Author(s) 2026. CC BY 4.0 License.

are also given in Table 2. There is very good agreement, as shown by the mean bias (MB) and root mean square error (RMSE). The correlation coefficient (COR) between CAMS AOTs and AOTs recalculated from mixing ratios is very significant with a value of 0.97.

Table 2: Specific cross sections σ_{spec} assessed for each aerosol compound using the CAMS data. The statistical parameters of the comparison between the AOTs provided by CAMS and those recalculated are also given: Mean bias (MB), root mean square error (RMSE) and corelation coefficient (COR).

	Dust	Carbonaceous	Soluble
σ_{spec} at 550 nm (m^2 g^{-1})	0.93	4.16	2.25
Statistical parameters on AOT at 550 nm	MB	RMSE	COR
	+5.7 10^{-3}	2.4 10^{-2}	0.97

4 Vertical profiles of aerosol layers

This section presents the results of the inversion of lidar profiles. As previously mentioned, the inversion is only performed during the nights between 23:00 and 05:00 UTC.

4.1 Night-to-night evolution of Lidar-derived aerosol optical properties

Figure 4 presents the temporal evolution of the vertical profiles of AEC (Figure 4a), PDR (Figure 4b) and LR (Figure 4c). Throughout the observation period, the lower troposphere (below 1-1.5 km a.m.s.l.) has been found to be the most aerosol–laden. AECs greater than 0.15 km^{-1} are frequently observed. However, these are not necessarily associated with high PDRs, despite the arid conditions around San Pedro Alcantara. On many profiles, layers with a PDR greater than 10% appear quickly as altitude increases up to ~7 km a.m.s.l.. They are indicative of the presence of dust-like particles, which are often found in such environments. As for PDR, LR varies greatly over time and along profiles. A wide range of LR values has been observed for dust or pollution aerosols (Mallet et al., 2022), particularly in the Mediterranean region. This diversity is obviously linked to the origin of the particles and their atmospheric ageing, as well as with air mass mixing. Note that when AEC is low (< ~0.02 km^{-1}), LR and PDR cannot be determined with sufficient accuracy.

https://doi.org/10.5194/egusphere-2026-765
Preprint. Discussion started: 11 March 2026
© Author(s) 2026. CC BY 4.0 License.

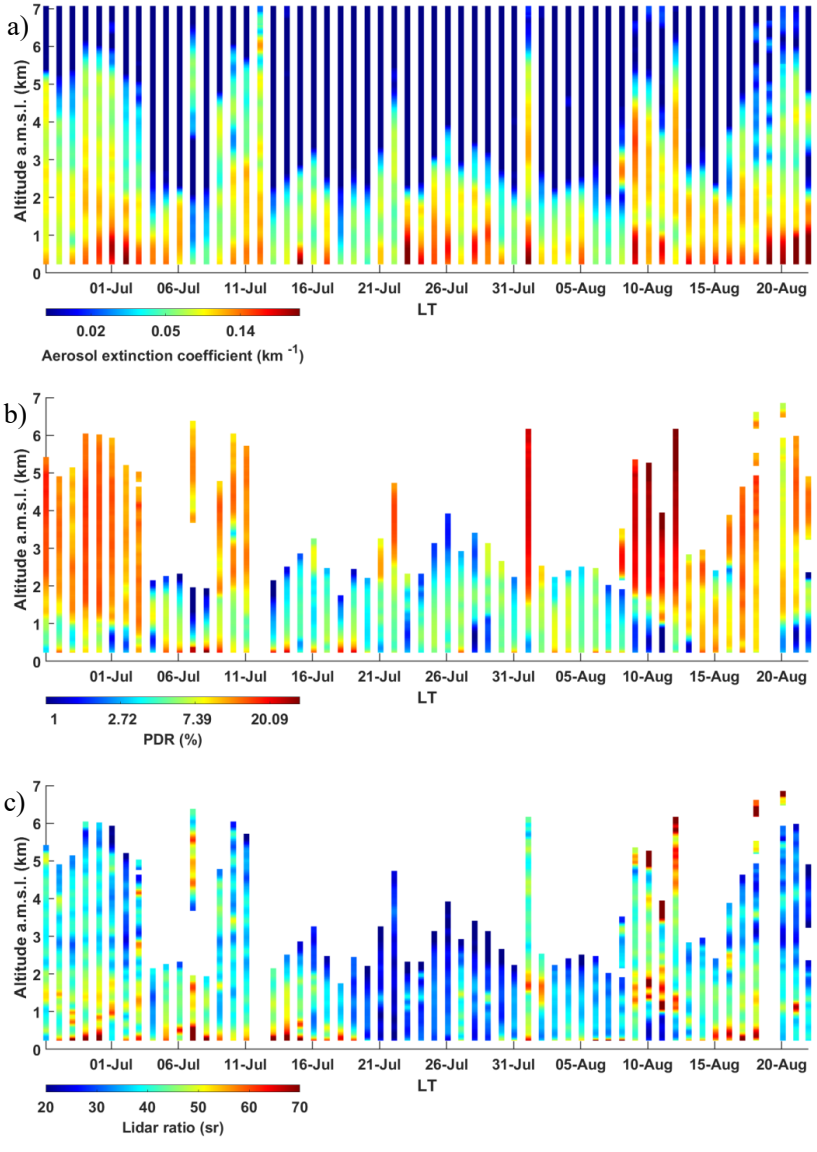

Figure 4. Temporal evolution of the mean night-time profiles derived from the N_2-Raman lidar is shown for a) the aerosol extinction coefficient, b) the linear particle depolarisation ratio (PDR), and c) the lidar ratio. The mean values are displayed for the period between 23:00 and 05:00 UTC on a nightly basis.

4.2 Highlight of aerosol classification by Raman lidar

In order to identify changes in aerosols more accurately over time and within the air column, it is best to rely on simultaneous LR and PDR measurements. The LR and PDR pair has been demonstrated to be the most discriminating technique for separating dusts, soluble and polluted aerosols. (Groß et al., 2013, 2015; Chazette et al., 2016a). Dust aerosols over the western

https://doi.org/10.5194/egusphere-2026-765
Preprint. Discussion started: 11 March 2026
© Author(s) 2026. CC BY 4.0 License.

Mediterranean Sea are attributable to the long-range transport of Saharan dust. These aerosols are typically linked with LRs between 30 and 80 sr (Papayannis et al., 2008), specifically for high PDRs, above 10% and up to ~30%. This variability is explained by the level of mixing with other aerosol types and the nature of soils in uplift areas. Marine aerosols have been found to have low LRs, ranging from 20 to 30 sr (Flamant et al., 1998), corresponding to a very low PDR of around 0%. These particles are frequently mixed with polluted aerosols or dust, thereby increasing their PDR and LR. Pollution and biomass fire aerosols also have highly variable LRs, depending on the source of combustion, but with values mostly above 60 sr. It should be noted that fire intensity, and therefore flame temperature, plays a role in LR values, as it influences the chemical composition of aerosols. In the event of strong thermal convection, terrigenous particles can also be lifted from the surface and may lead to LRs of the order of 8% (Chazette et al., 2016a), whereas they are rather of the order of 2-3% for young aerosols and more than double when they are older following long-range transport (Mallet et al., 2022).

Taking the above into account, the following colour combination is proposed to help identify the three distinct aerosol types and their potential for mixing by using two-dimensional normal distributions (C). The first dimension is defined on the PDR and the second on the LR. For each primary colour (red, green, and blue):

$$C = \frac{1}{2 \cdot \pi \cdot \sigma_{PDR} \cdot \sigma_{LR}} \cdot e^{-\frac{1}{2}\left[\frac{(PDR-PDR_o)^2}{\sigma_{PDR}^2}+\frac{(LR-LR_o)^2}{\sigma_{LR}^2}\right]} \quad (10)$$

The PDR_o and LR_o (σ_{PDR} and σ_{LR}) values in Table 3 are assigned to the mean values (standard deviations) of PDR and LR. These values consider the possible ranges of PDR and LR for each aerosol type. Figure 5 shows the temporal evolution of the three aerosol classes and highlights their potential mixing, revealing a strong presence of dust particles (red trend) at the beginning and end of the field campaign. All the main dust contributions are due to Saharan air mass transport, which is well highlighted on MODIS and SEVIRI (Spinning Enhanced Visible and Infra-Red Imager) aerosol products (e.g. see https://worldview.earthdata.nasa.gov/, last access: 24 January 2026). These particles mix with the other types of aerosols in the lower layers below 1.5 km above sea level, where pollution events (green trend) can be observed alongside the marine contributions (blue trend). Local occurrence is not a prerequisite for these mixtures; instead, they are primarily linked to the long-range transport of aerosol plumes of diverse origins by convergent dynamic processes.

https://doi.org/10.5194/egusphere-2026-765
Preprint. Discussion started: 11 March 2026
© Author(s) 2026. CC BY 4.0 License.

Table 3. Mean linear particle depolarization ratio (PDR_o) and lidar ratio (LR_o) for each aerosol type, along with their respective standard deviations (σ_{PDR} and σ_{LR}).

Aerosol type	PDR_o (%)	σ_{PDR} (%)	LR_o (sr)	σ_{LR} (sr)
Dust-like	20	10	50	20
Marin-like	2	6	30	10
Pollution-like	7	6	60	20

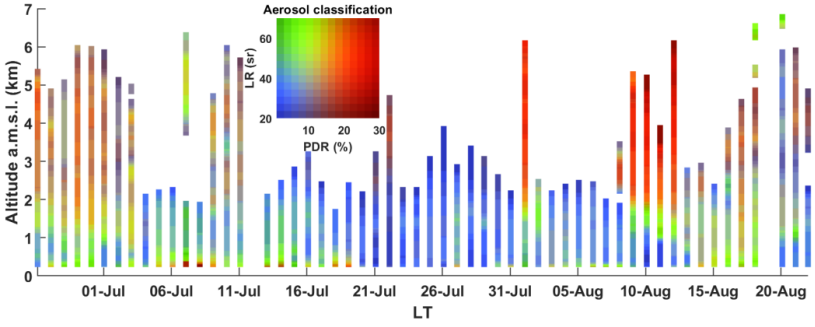

Figure 5. Temporal evolution of the aerosol classification performed using the linear particle depolarisation ratio (PDR) and the lidar ratio (LR). Aerosols of marine origin tend towards blue, pollution aerosols towards green, and terrigenous aerosols towards red.

4.3 Comparison with sun photometer measurements

During day, sun photometer measurements provide information on the nature of the aerosols present in the air. Angstrom exponents of less than 0.5, which are associated with higher optical thicknesses (Figure 3) are generally indicative of dust events. Saharan dust events with AOT > 0.6 are clearly highlighted by photometric measurements during the following periods in 2011: 26 June–4 July, 8–12 July, 20–22 July, 8–12 August and sporadically from 16 to 22 August. Their origin is mainly located between Morocco and Algeria, towards the great western erg (Chazette, 2020). In June, their origin is more distant, with a plausible source located in northern Mauritania as highlighted from airborne measurements (Ryder et al., 2015). The plume has recirculated over the Atlantic before entering the Mediterranean via Gibraltar. Note that on 25 July, the AOT reached 0.7 for A~1.4 during the day, which was not detected by the lidar during the night. This is characteristic of pollution or biomass burning aerosols.

5 Consistency with CAMS simulations

Lidar measurements do not allow for quantitative separation of the optical contributions of each aerosol compounds. Consistency between lidar measurements and CAMS data can therefore only be achieved for the total aerosol contribution. The total AOTs are provided directly via the CAMS database whereas, as explained in subsection 3.2, the vertical extinction profiles must be evaluated using the available mixing ratios in the database.

5.1 Aerosol optical thickness

https://doi.org/10.5194/egusphere-2026-765
Preprint. Discussion started: 11 March 2026
© Author(s) 2026. CC BY 4.0 License.

Figure 6 shows the temporal evolution of AOTs derived from CAMS reanalyses for each type of bulk aerosol composition at the ground-based site. The five Saharan dust events previously identified are clearly visible.

There are two approaches to comparing AOTs. The first consists of doing so at a wavelength of 550 nm by converting the lidar-derived AOTs to the same wavelength. To do this, an interpolation of the Ångström exponents retrieved from the sun photometer is used (red curve in Figure 3). The AOTs derived from the lidar measurements and the sun photometer are also shown in Figure 6. The second method consists of bringing the AOTs derived from the model to the lidar wavelength using the Ångström exponent predicted by CAMS. The statistical results of these two approaches are shown at the top of Table 4.

For both approaches, there is a very small underestimation of the total AOT by CAMS (-0.01) compared to lidar. The CORs are very similar, with values exceeding 0.83. This tends to show that CAMS satisfactorily reproduces the variability of integrated aerosol content throughout the lidar measurement period. The RMSEs are greater at 355 nm (~0.09) than at 550 nm (~0.06). This difference can be explained by the inclusion of an Ångström exponent from the modelling. This exponent introduces additional uncertainties possibly related to poor prediction of the size distribution and/or chemical composition of aerosols. When comparisons are made at 550 nm, the uncertainties are lower because the interpolation of sun photometer measurements taken at night is more likely to reflect reality. Hence, working at the lidar wavelength of 355 nm better highlights the differences between the lidar observation and the CAMS products.

It is important to note that achieving a satisfactory score for total optical thickness does not necessarily guarantee the same level of quality for profiles.

Table 4: Statistical parameters of the comparison between the aerosol optical thicknesses derived from the Raman lidar and the corresponding CAMS products (lidar-CAMS): Mean bias (MB), root mean square error (RMSE) and correlation coefficient (COR).

Comparison wavelength	MB	RMSE	COR
550 nm	-0.01	0.064	0.89
355 nm	-0.01	0.093	0.83
	Statistical parameters at 355 nm		
Layers			
~0.57 – 2 km	+0.06	0.05	0.56
~2 – 7 km	-0.01	0.05	0.87

https://doi.org/10.5194/egusphere-2026-765
Preprint. Discussion started: 11 March 2026
© Author(s) 2026. CC BY 4.0 License.

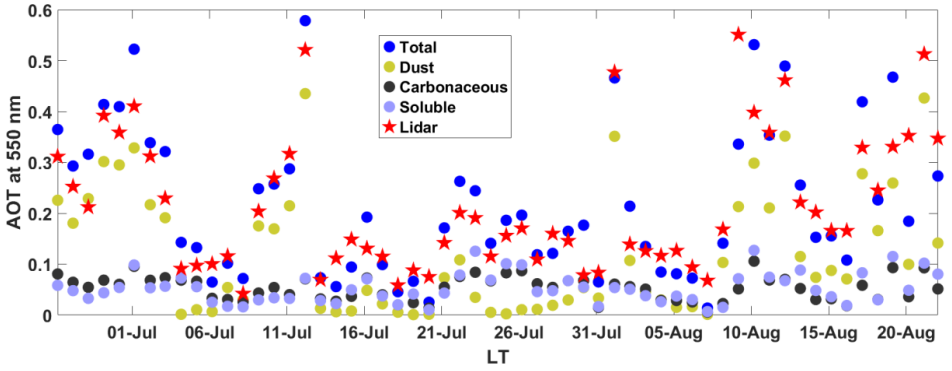

Figure 6. Superimposition of the temporal evolution of the aerosol optical thickness (AOT) derived from CAMS (total aerosol contribution and, dust, carbonaceous and soluble compounds) and from the N_2–Raman lidar at 550 nm.

5.2 Vertical profile of the aerosol extinction coefficient

The same statistical study was carried out on the AEC for the different altitude levels of CAMS products at the wavelength of 355 nm, which is more appropriate for assessing the reliability of modelling.

The result is shown in Figure 7. The MB varies significantly with altitude. It is positive near the surface and slightly negative above, where desert aerosol layers are predominantly located. The RMSE is significantly higher near the surface. This is associated with fairly low CORs (~0.4), showing that CAMS products find it more difficult to represent what is happening in the planetary boundary layer (PBL). In the upper layers, the COR reaches values slightly above 0.8, indicating that modelling accurately reproduces the temporal variability of desert aerosol plumes. Table 4 summarises these results in terms of AOT in two layers: the lower layer, which is below 2 km a.m.s.l. and the layer containing mainly desert aerosols, which is located between 2 and 7 km a.m.s.l. As shown on the vertical profiles, the most notable difference is in the COR: it averages 0.56 in the lower layer and 0.9 in the upper layer. There is also a significant positive bias in the lower layer (+0.06), indicating an underestimation by CAMS products. This may be linked to errors in emissions that can be directly attributed to the emission register, and/or the more complex dynamics of the lower layer in coastal regions.

The apparent loss of correlation between the results on the profiles and the total AOT is most certainly linked to the incorrect positioning of the aerosol layers in terms of altitude in CAMS. This positioning can fluctuate greatly over time, particularly between periods with and without long-distance transport events. It is more difficult to quantify this aspect statistically in this

https://doi.org/10.5194/egusphere-2026-765
Preprint. Discussion started: 11 March 2026
© Author(s) 2026. CC BY 4.0 License.

campaign because, even though it lasted approximately two months, there were not enough transitions sampled from one transport regime to another.

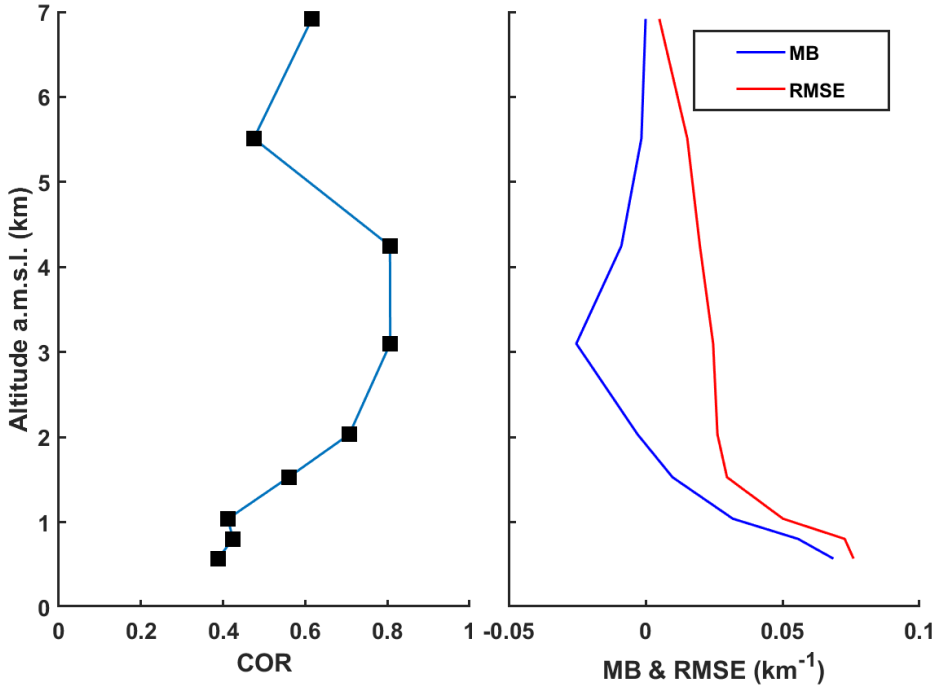

Figure 7: Statistical parameters calculated on the first nine altitude levels of CAMS when comparing lidar measurements with CAMS products at 355 nm. The vertical profiles show: a) the correlation coefficient (COR) and b) the mean bias (MB, lidar - CAMS) and the root mean square error (RMSE) on the aerosol extinction coefficient.

5.3 Aerosol identification

Figure 8 shows the temporal evolution of the mass mixing ratios of the three bulk aerosol compositions, as derived from the CAMS reanalysis. Qualitatively, The altitude and time locations of the dust plume (Figure 8a) correspond to the optical apportionment of the aerosols derived from LAASURS (Figure 5). This demonstrates that CAMS reanalyses provide an excellent representation of mesoscale aerosol transport, uplift and dispersion processes. Polluted aerosols (Figure 8b) are also well represented in terms of their temporal and vertical extent. Between 21 and 31 July, a slightly more marine trend emerges (Figure 8c), which could be classified as “dusty marine”. During this period under 1.5 km a.m.s.l., the composition of the aerosols appears to be a variable mixture of dust, carbonaceous and soluble compounds. This results in a range of intermediate values for both the LR and the PDR. In the Mediterranean region, the likelihood of desert aerosols combining with other atmospheric particles explains

https://doi.org/10.5194/egusphere-2026-765
Preprint. Discussion started: 11 March 2026
© Author(s) 2026. CC BY 4.0 License.

the variability of the LR observed in different locations within the basin (Mallet et al., 2022; Papayannis et al., 2008).

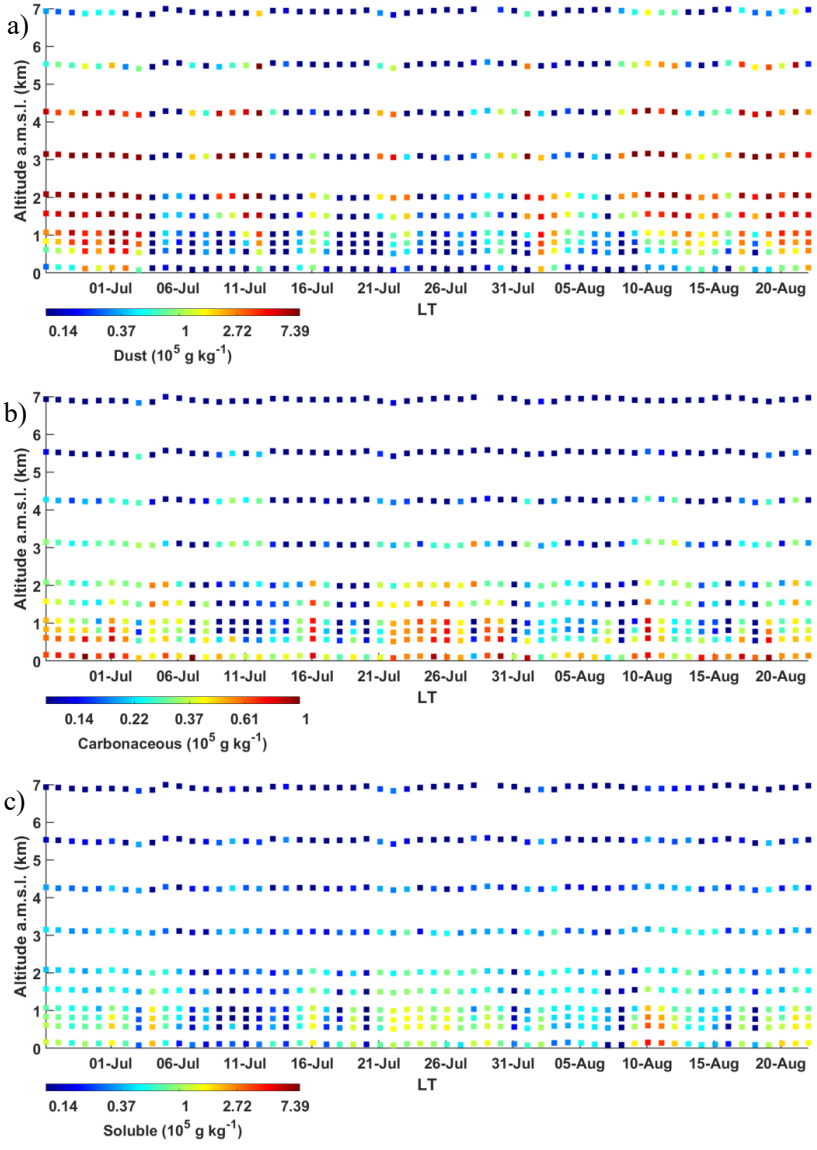

Figure 8. Temporal evolution of the profiles of mass mixing ratios derived from CAMS nearest night-time is shown for the following aerosol compounds: a) the soluble (sea salt and sulphate), b) dust, and c) carbonaceous (black and organic carbon). The vertical resolution is that of the CAMS products.

The correspondence between lidar and CAMS for identifying aerosol types is clearly shown in the ternary diagrams in Figure 9. For each time period and CAMS level, the LR (Figure 9a) and

https://doi.org/10.5194/egusphere-2026-765
Preprint. Discussion started: 11 March 2026
© Author(s) 2026. CC BY 4.0 License.

PDR (Figure 9b) are displayed using a colour scale. On these diagrams, pure compounds are located at the vertices of the equilateral rectangle. Most high PDR values correspond to points close to the "dust" vertex of the rectangle (CAMS estimates over 60% "dust"), and are mainly associated with intermediate LR values (approximately 45 sr), as is often found in the literature (e.g. Papayannis et al., 2005). The contribution of carbonaceous compounds to the composition of aerosols is significantly lower than that of soluble compounds. Nevertheless, these diagrams clearly show that the three components are often mixed. It should be noted that there were no significant biomass fires in Andalusia during the summer of 2011.

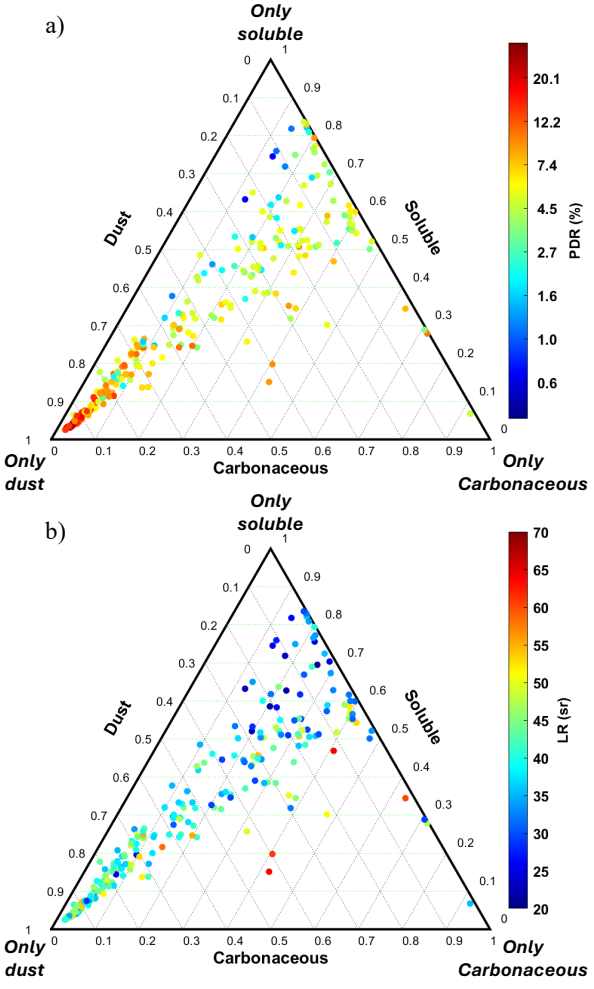

https://doi.org/10.5194/egusphere-2026-765
Preprint. Discussion started: 11 March 2026
© Author(s) 2026. CC BY 4.0 License.

Figure 9. Ternary diagram established from the aerosol compounds derived from CAMS: dust, carbonaceous and soluble compounds. Each colour dot corresponds to lidar-derived optical properties: a) particulate depolarization ratio (PDR) and b) lidar ratio (LR).

6 Conclusion

Considerable progress has been made in modelling aerosol transport since the FENNEC campaign in 2011. This has been accomplished through more accurate inventories of aerosol sources and improving the spatial resolution of the models, particularly in the vertical dimension. However, additional experimental validation methods are needed to increase confidence in modelling. This should primarily involve using resolved measurements taken directly in the atmospheric column, such as those provided by lidar. Consequently, the data acquired from the ground-based site in San Pedro Alcantara from June to August 2011 provide a unique opportunity to compare the CAMS reanalyses with the optical products of the LAASURS N_2–Raman lidar at 355 nm. During the FENNEC programme, LAASURS monitored aerosols with high vertical resolution (100 m). This monitoring aimed to accurately locate the transport of Saharan aerosols in southern Spain, assess their frequency and intensity, and analyse how they mix with other, more local, aerosol layers. The PDR and LR pairs were derived from night-time measurements to ensure the lidar range sampled the desert aerosol layers above 7 km a.m.s.l. This makes it possible to identify the aerosols and their mixtures in the vertical profiles.

The CAMS reanalyses were found to be in very good agreement with the geophysical products derived from optical lidar measurements for dust layers. This is particularly notable for the AOTs. The reanalyses accurately reproduce dust events in terms of both time and vertical expends with COR larger than 0.8. There is an agreement of between 10 and 20% on the total AOTs mainly driven by dust aerosols. The mixing of pollution (characterised by the carbonaceous component) with marine (characterised by the soluble component) and dust contributions is also accurately reproduced throughout the two-month experiment. Nevertheless, the correlation observed between lidar measurements and CAMS reanalyses for the atmospheric layer below 2 km a.m.s.l. is significantly lower (0.56). It is associated with an underestimation of the contribution to the AOT of this layer of around 0.06, which may be due to an incorrect assessment of emission processes.

These results show that assimilating lidar measurements can impose significant constraints on aerosol transport models (Wang et al., 2013, 2014b). This is an important area on which to focus on, given the current risks for the climate and air quality. Note that the optical aerosol classification technique used here for a single-wavelength Raman lidar at 355 nm can also be

https://doi.org/10.5194/egusphere-2026-765
Preprint. Discussion started: 11 March 2026
© Author(s) 2026. CC BY 4.0 License.

used with a high spectral resolution lidar, such as the Atmospheric Lidar (ATLID) of the Earth Clouds, Aerosols and Radiation Explorer mission (EarthCARE, https://earth.esa.int/eogateway/missions/earthcare, last access: 5 February 2026).

Appendix A: Statistical parameters

The statistical indicators used to evaluate the consistency between lidar-derived ($\alpha_{a,lidar}$) and CAMS-derived ($\alpha_{a,cams}$) AEC are the mean bias (MB), the root mean square error (RMSE) and the (Pearson) correlation (COR). These metrics are commonly used to assess model performance (Boylan and Russell, 2006; Tombette et al., 2008). For a given time *t* and altitude *z*, the MB is given by the following relationship:

$$MB(z) = \langle \alpha_{a,lidar}(\mathrm{t},\mathrm{z}) \rangle - \langle \alpha_{a,cams}(\mathrm{t},\mathrm{z}) \rangle \quad \text{(A1)}$$

The RMSE is given by:

$$RMSE(z) = \sqrt{RMSD^2 - MB^2} \quad \text{(A2)}$$

with the root mean square difference (RMSD) given by:

$$RMSD(z) = \sqrt{\langle \left(\alpha_{a,lidar}(\mathrm{t},\mathrm{z}) - \alpha_{a,cams}(\mathrm{t},\mathrm{z}) \right)^2 \rangle} \quad \text{(A3)}$$

The COR is expressed as follows:

$$COR(z) = \frac{\langle \left(\alpha_{a,lidar}(\mathrm{t},\mathrm{z}) - \langle \alpha_{a,lidar}(\mathrm{t},\mathrm{z}) \rangle \right) \cdot \left(\alpha_{a,cams}(\mathrm{t},\mathrm{z}) - \langle \alpha_{a,cams}(\mathrm{t},\mathrm{z}) \rangle \right) \rangle}{\sqrt{\langle \left(\alpha_{a,lidar}(\mathrm{t},\mathrm{z}) - \langle \alpha_{a,lidar}(\mathrm{t},\mathrm{z}) \rangle \right)^2 \rangle \cdot \langle \left(\alpha_{a,cams}(\mathrm{t},\mathrm{z}) - \langle \alpha_{a,cams}(\mathrm{t},\mathrm{z}) \rangle \right)^2 \rangle}} \quad \text{(A4)}$$

The AOTs can also be treated with the same equations by replacing the AEC with the respective AOTs.

Data availability. All data sets have been downloaded from the respective model websites.

Competing interests. The author declares that he has no conflict of interest.

Acknowledgements. This work was supported by the Centre National d'Études Spatiales (CNES) and by the Commissariat à l'Energie Atomique et aux Énergies Alternatives (CEA). Cyrille Flamant, Joseph Sanak, Fabien Marnas and Philippe Royer are acknowledged for their help in building and implementing the field experiment. The author would like to thank the AERONET network for sun photometer products (at https://aeronet.gsfc.nasa.gov/), the MODIS Science, Processing and Data Support Teams for producing and providing MODIS

https://doi.org/10.5194/egusphere-2026-765
Preprint. Discussion started: 11 March 2026
© Author(s) 2026. CC BY 4.0 License.

data (at https://modis.gsfc.nasa.gov/data/dataprod/), and the NASA Langley Research Center Atmospheric Sciences Data Center for the data processing and distribution of CALIPSO products (level 4.10, at https://eosweb.larc.nasa.gov/HORDERBIN/HTML_Start.cgi). The NOAA Air Resources Laboratory (ARL) is acknowledged for the provision of the HYSPLIT transport and dispersion model and READY website (http://www.ready.noaa.gov) used in this publication. The ERA5 dataset is provided by the ECMWF integrated forecast system, developed through the Copernicus Climate Change Service (https://climate.copernicus.eu/, last access: 24 January 2026).

References

Ångström, A.: The parameters of atmospheric turbidity, Tellus A, 16, 64–75, https://doi.org/10.3402/tellusa.v16i1.8885, 1964.

Barragan, R., Sicard, M., Totems, J., Léon, J. F. F., Dulac, F., Mallet, M., Pelon, J., Alados-Arboledas, L., Amodeo, A., Augustin, P., Boselli, A., Bravo-Aranda, J. A. A., Burlizzi, P., Chazette, P., Comerón, A., D'Amico, G., Dubuisson, P., Granados-Muñoz, M. J. J., Leto, G., Guerrero-Rascado, J. L. L., Madonna, F., Mona, L., Muñoz-Porcar, C., Pappalardo, G., Perrone, M. R. R., Pont, V., Rocadenbosch, F., Rodriguez-Gomez, A., Scollo, S., Spinelli, N., Titos, G., Wang, X., and Sanchez, R. Z. Z.: Spatio-temporal monitoring by ground-based and air- and space-borne lidars of a moderate Saharan dust event affecting southern Europe in June 2013 in the framework of the ADRIMED/ChArMEx campaign, Air Qual. Atmos. Heal., 10, 261–285, https://doi.org/10.1007/s11869-016-0447-7, 2017.

Bellouin, N., Quaas, J., Gryspeerdt, E., Kinne, S., Stier, P., Watson-Parris, D., Boucher, O., Carslaw, K. S., Christensen, M., Daniau, A. L., Dufresne, J. L., Feingold, G., Fiedler, S., Forster, P., Gettelman, A., Haywood, J. M., Lohmann, U., Malavelle, F., Mauritsen, T., McCoy, D. T., Myhre, G., Mülmenstädt, J., Neubauer, D., Possner, A., Rugenstein, M., Sato, Y., Schulz, M., Schwartz, S. E., Sourdeval, O., Storelvmo, T., Toll, V., Winker, D., and Stevens, B.: Bounding Global Aerosol Radiative Forcing of Climate Change, https://doi.org/10.1029/2019RG000660, 1 March 2020.

Benedetti, A., Morcrette, J. J., Boucher, O., Dethof, A., Engelen, R. J., Fisher, M., Flentje, H., Huneeus, N., Jones, L., Kaiser, J. W., Kinne, S., Mangold, A., Razinger, M., Simmons, A. J., and Suttie, M.: Aerosol analysis and forecast in the European Centre for Medium-Range Weather Forecasts integrated forecast system: 2. data assimilation, J. Geophys. Res. Atmos., 114, D13205, https://doi.org/10.1029/2008JD011115, 2009.

Boylan, J. W. and Russell, A. G.: PM and light extinction model performance metrics, goals, and criteria for three-dimensional air quality models, Atmos. Environ., 40, 4946–4959, 2006.
Chazette, P.: Aerosol optical properties as observed from an ultralight aircraft over the Strait of Gibraltar, Atmos. Meas. Tech. Discuss., 2011, 1–24, https://doi.org/10.5194/amt-2020-131, 2020.

Chazette, P., Dabas, A., Sanak, J., Lardier, M., and Royer, P.: French airborne lidar measurements for Eyjafjallajökull ash plume survey, Atmos. Chem. Phys., 12, 7059–7072, https://doi.org/10.5194/acp-12-7059-2012, 2012.

https://doi.org/10.5194/egusphere-2026-765
Preprint. Discussion started: 11 March 2026
© Author(s) 2026. CC BY 4.0 License.

Chazette, P., Marnas, F., and Totems, J.: The mobile Water vapor Aerosol Raman LIdar and its implication in the framework of the HyMeX and ChArMEx programs: application to a dust transport process, Atmos. Meas. Tech., 7, 1629–1647, https://doi.org/10.5194/amt-7-1629-2014, 2014.

Chazette, P., Totems, J., Ancellet, G., Pelon, J., and Sicard, M.: Temporal consistency of lidar observations during aerosol transport events in the framework of the ChArMEx/ADRIMED campaign at Minorca in June 2013, Atmos. Chem. Phys., 16, 2863–2875, https://doi.org/10.5194/acp-16-2863-2016, 2016a.

Chazette, P., Flamant, C., Raut, J.-C., Totems, J., and Shang, X.: Tropical moisture enriched storm tracks over the Mediterranean and their link with intense rainfall in the Cevennes-Vivarais area during HyMeX, Q. J. R. Meteorol. Soc., 142, https://doi.org/10.1002/qj.2674, 2016b.

Chazette, P., Totems, J., and Shang, X.: Transport of aerosols over the French Riviera-link between ground-based lidar and spaceborne observations, Atmos. Chem. Phys., 19, 3885–3904, https://doi.org/10.5194/acp-19-3885-2019, 2019.

Collis, R. T. H. and Russel, P. B.: Lidar measurement of particles and gases by elastic backscattering and differential absorption in Laser Monitoring of the Atmosphere, edited by: Hinkley, E. D., Springer Berlin Heidelberg, Berlin, Heidelberg, 71–152 pp., https://doi.org/10.1007/3-540-07743-X, 1976.

Dieudonné, E., Chazette, P., Marnas, F., Totems, J., and Shang, X.: Lidar profiling of aerosol optical properties from Paris to Lake Baikal (Siberia), Atmos. Chem. Phys., 15, 5007–5026, https://doi.org/doi:10.5194/acp-15-5007-2015, 2015.

Dieudonné, E., Chazette, P., Marnas, F., Totems, J., and Shang, X.: Raman Lidar Observations of Aerosol Optical Properties in 11 Cities from France to Siberia, Remote Sens., 9, 978–1007, https://doi.org/10.3390/rs9100978, 2017.

Dubovik, O. and King, M. D.: A flexible inversion algorithm for retrieval of aerosol optical properties from Sun and sky radiance measurements, J. Geophys. Res. Atmos., 105, 20673–20696, https://doi.org/10.1029/2000JD900282, 2000.

Dulac, F. and Chazette, P.: Airborne study of a multi-layer aerosol structure in the eastern Mediterranean observed with the airborne polarized lidar ALEX during a STAAARTE campaign (7 June 1997), Atmos. Chem. Phys., 3, 1817–1831, https://doi.org/10.5194/acp-3-1817-2003, 2003.

Flamant, C., Trouillet, V., Chazette, P., and Pelon, J.: Wind speed dependence of atmospheric boundary layer optical properties and ocean surface reflectance as observed by airborne backscatter lidar, J. Geophys. Res. Ocean., 103, 25137–25158, https://doi.org/10.1029/98JC02284, 1998.

Flamant, C., Chaboureau, J.-P., Chazette, P., Di Girolamo, P., Bourrianne, T., Totems, J., and Cacciani, M.: The radiative impact of desert dust on orographic rain in the Cévennes-Vivarais area: A case study from HyMeX, Atmos. Chem. Phys., 15, https://doi.org/10.5194/acp-15-

https://doi.org/10.5194/egusphere-2026-765
Preprint. Discussion started: 11 March 2026
© Author(s) 2026. CC BY 4.0 License.

12231-2015, 2015.

Forster, P., Ramaswamy, V., Artaxo, P., Berntsen, T., and Betts, R.: Changes in atmospheric constituents and in radiative forcing, in: Climate Change 2007: The Physical Science Basis. Contribution of Working Group I to the Fourth Assessment Report of the Intergovernmental Panel on Climate Change, edited by: Solomon, S., Qin, D., Manning, M., Chen, Z., Marquis, M., Averyt, K. B., Tignor, M., and Miller, H. L., United Kingdom and New York, NY, USA, 129–234, 2007.

Fourrié, N., Nuret, M., Brousseau, P., Caumont, O., Doerenbecher, A., Wattrelot, E., Moll, P., Bénichou, H., Puech, D., Bock, O., Bosser, P., Chazette, P., Flamant, C., Di Girolamo, P., Richard, E., and Saïd, F.: The AROME-WMED reanalyses of the first special observation period of the Hydrological cycle in the Mediterranean experiment (HyMeX), Geosci. Model Dev., 12, 2657–2678, https://doi.org/10.5194/gmd-12-2657-2019, 2019.

Gallero, F. J. G., Vallejo, M. G., Umbría, A., and Baena, J. G.: Multivariate statistical analysis of meteorological and air pollution data in the “Campo De Gibraltar” Region, Spain, Environ. Monit. Assess., 119, 405–423, https://doi.org/10.1007/s10661-005-9033-4, 2006.

Ghan, S. J.: Technical note: Estimating aerosol effects on cloud radiative forcing, Atmos. Chem. Phys., 13, 9971–9974, https://doi.org/10.5194/acp-13-9971-2013, 2013.

Giorgi, F. and Lionello, P.: Climate change projections for the Mediterranean region, Glob. Planet. Change, 63, 90–104, https://doi.org/10.1016/j.gloplacha.2007.09.005, 2008.

Di Girolamo, P., De Rosa, B., Flamant, C., Summa, D., Bousquet, O., Chazette, P., Totems, J., and Cacciani, M.: Water vapor mixing ratio and temperature inter-comparison results in the framework of the Hydrological Cycle in the Mediterranean Experiment—Special Observation Period 1, Bull. Atmos. Sci. Technol., 1, 113–153, https://doi.org/10.1007/s42865-020-00008-3, 2020.

Groß, S., Esselborn, M., Weinzierl, B., Wirth, M., Fix, A., and Petzold, A.: Aerosol classification by airborne high spectral resolution lidar observations, Atmos. Chem. Phys., 13, 2487–2505, https://doi.org/10.5194/acp-13-2487-2013, 2013.

Groß, S., Freudenthaler, V., Wirth, M., and Weinzierl, B.: Towards an aerosol classification scheme for future EarthCARE lidar observations and implications for research needs, Atmos. Sci. Lett., 16, 77–82, https://doi.org/10.1002/asl2.524, 2015.

Hamonou, E., Chazette, P., Balis, D., Dulac, F., Schneider, X., Galani, E., Ancellet, G., and Papayannis, A.: Characterization of the vertical structure of Saharan dust export to the Mediterranean basin, J. Geophys. Res., 104, 22257, https://doi.org/10.1029/1999JD900257, 1999.

Hersbach, H., Bell, B., Berrisford, P., Hirahara, S., Horányi, A., Muñoz-Sabater, J., Nicolas, J., Peubey, C., Radu, R., Schepers, D., Simmons, A., Soci, C., Abdalla, S., Abellan, X., Balsamo, G., Bechtold, P., Biavati, G., Bidlot, J., Bonavita, M., De Chiara, G., Dahlgren, P., Dee, D., Diamantakis, M., Dragani, R., Flemming, J., Forbes, R., Fuentes, M., Geer, A., Haimberger, L., Healy, S., Hogan, R. J., Hólm, E., Janisková, M., Keeley, S., Laloyaux, P., Lopez, P., Lupu, C., Radnoti, G., de Rosnay, P., Rozum, I., Vamborg, F., Villaume, S., and Thépaut, J. N.: The

https://doi.org/10.5194/egusphere-2026-765
Preprint. Discussion started: 11 March 2026
© Author(s) 2026. CC BY 4.0 License.

ERA5 global reanalysis, Q. J. R. Meteorol. Soc., 146, 1999–2049, https://doi.org/10.1002/qj.3803, 2020.

Huneeus, N., Chevallier, F., and Boucher, O.: Estimating aerosol emissions by assimilating observed aerosol optical depth in a global aerosol model, Atmos. Chem. Phys., 12, 4585–4606, https://doi.org/10.5194/acp-12-4585-2012, 2012.

Inness, A., Ades, M., Agustí-Panareda, A., Barr, J., Benedictow, A., Blechschmidt, A. M., Jose Dominguez, J., Engelen, R., Eskes, H., Flemming, J., Huijnen, V., Jones, L., Kipling, Z., Massart, S., Parrington, M., Peuch, V. H., Razinger, M., Remy, S., Schulz, M., and Suttie, M.: The CAMS reanalysis of atmospheric composition, Atmos. Chem. Phys., 19, 3515–3556, https://doi.org/https://doi.org/10.5194/acp-19-3515-2019, 2019.

IPCC: Climate change 2022: Impacts, Adaptation and Vulnerability. Summary for policymakers. Contribution of Working Group II to the Sixth Assessment Report of the Intergovernmental Panel on Climate Change, in: United Nations Environment Programme UNEP, vol. AR6, Cambridge University Press, 551–712, 2022.

Kaufman, Y. J., Tanré, D., and Boucher, O.: A satellite view of aerosols in the climate system, Nature, 419, 215–223, https://doi.org/10.1038/nature01091, 2002.

Mallet, M., Dulac, F., Formenti, P., Nabat, P., Sciare, J., Roberts, G., Pelon, J., Ancellet, G., Tanré, D., Parol, F., Di Sarra, A., Alados, L., Arndt, J., Auriol, F., Blarel, L., Bourrianne, T., Brogniez, G., Chazette, P., Chevaillier, S., Claeys, M., D'Anna, B., Denjean, C., Derimian, Y., Desboeufs, K., Di Iorio, T., Doussin, J.-F., Durand, P., Féron, A., Freney, E., Gaimoz, C., Goloub, P., Gómez-Amo, J. L., Granados-Muñoz, M. J., Grand, N., Hamonou, E., Jankowiak, I., Jeannot, M., Léon, J.-F., Maillé, M., Mailler, S., Meloni, D., Menut, L., Momboisse, G., Nicolas, J., Podvin, J., Pont, V., Rea, G., Renard, J.-B., Roblou, L., Schepanski, K., Schwarzenboeck, A., Sellegri, K., Sicard, M., Solmon, F., Somot, S., Torres, B., Totems, J., Triquet, S., Verdier, N., Verwaerde, C., Wenger, J., and Zapf, P.: Overview of the Chemistry-Aerosol Mediterranean Experiment/Aerosol Direct Radiative Forcing on the Mediterranean Climate (ChArMEx/ADRIMED) summer 2013 campaign, Atmos. Chem. Phys. Discuss., 15, https://doi.org/10.5194/acpd-15-19615-2015, 2015.

Mallet, M., Chazette, P., Dulac, F., Formenti, P., Di Biagio, C., Denjean, C., and Chiapello, I.: Aerosol optical properties, in: Atmospheric chemistry in the Mediterranean, edited by: Dulac, F., Sauvage, S., and Hamonou, E., 32 pp., https://doi.org/https://doi.org/10.1007/978-3-03082385-6_14, 2022.

Measures, R. M.: Laser remote sensing: fundamentals and applications, edited by: Wiley, J., Krieger publishing company: Malabar, FL, USA, 510 pp., 1984.

Nabat, P., Somot, S., Mallet, M., Sevault, F., Chiacchio, M., and Wild, M.: Direct and semi-direct aerosol radiative effect on the Mediterranean climate variability using a coupled regional climate system model, Clim. Dyn., 44, 1127–1155, https://doi.org/10.1007/s00382-014-2205-6, 2015.

Navas-Guzmán, F., Bravo-Aranda, J. A., Guerrero-Rascado, J. L., Granados-Muñoz, M. J., and Alados-Arboledas, L.: Statistical analysis of aerosol optical properties retrieved by Raman lidar over Southeastern Spain, Tellus, Ser. B Chem. Phys. Meteorol., 65,

https://doi.org/10.5194/egusphere-2026-765
Preprint. Discussion started: 11 March 2026
© Author(s) 2026. CC BY 4.0 License.

https://doi.org/10.3402/tellusb.v65i0.21234, 2013.

Nicolet, M.: On the molecular scattering in the terrestrial atmosphere : An empirical formula for its calculation in the homosphere, Planet. Space Sci., 32, 1467–1468, https://doi.org/10.1016/0032-0633(84)90089-8, 1984.

Papayannis, A., Balis, D., Amiridis, V., Chourdakis, G., Tsaknakis, G., Zerefos, C., Castanho, A. D. A., Nickovic, S., Kazadzis, S., and Grabowski, J.: Measurements of Saharan dust aerosols over the eastern Mediterranean using elastic backscatter-Raman lidar, spectrophotometric and satellite observations in the frame of the EARLINET project, Atmos. Chem. Phys., 5, 2065–2079, https://doi.org/10.5194/acp-5-2065-2005, 2005.

Papayannis, A., Amiridis, V., Mona, L., Tsaknakis, G., Balis, D., Bösenberg, J., Chaikovski, A., De Tomasi, F., Grigorov, I., Mattis, I., Mitev, V., Müller, D., Nickovic, S., Pérez, C., Pietruczuk, A., Pisani, G., Ravetta, F., Rizi, V., Sicard, M., Trickl, T., Wiegner, M., Gerding, M., Mamouri, R. E., D'Amico, G., and Pappalardo, G.: Systematic lidar observations of Saharan dust over Europe in the frame of EARLINET (2000–2002), J. Geophys. Res. Atmos., 113, D10204, https://doi.org/10.1029/2007JD009028, 2008.

Remer, L. A., Kaufman, Y. J., Tanré, D., Mattoo, S., Chu, D. A., Martins, J. V., Li, R.-R., Ichoku, C., Levy, R. C., Kleidman, R. G., Eck, T. F., Vermote, E., and Holben, B. N.: The MODIS Aerosol Algorithm, Products, and Validation, J. Atmos. Sci., 62, 947–973, https://doi.org/10.1175/JAS3385.1, 2005.

Rodríguez, S., Querol, X., Alastuey, A., Kallos, G., and Kakaliagou, O.: Saharan dust contributions to PM10 and TSP levels in Southern and Eastern Spain, Atmos. Environ., 35, 2433–2447, https://doi.org/10.1016/S1352-2310(00)00496-9, 2001.

Royer, P., Chazette, P., Lardier, M., and Sauvage, L.: Aerosol content survey by mini N2-Raman lidar: Application to local and long-range transport aerosols, Atmos. Environ., 45, 7487–7495, https://doi.org/10.1016/j.atmosenv.2010.11.001, 2011a.

Royer, P., Chazette, P., Sartelet, K., Zhang, Q. J., Beekmann, M., and Raut, J. C.: Comparison of lidar-derived PM10 with regional modeling and ground-based observations in the frame of MEGAPOLI experiment, Atmos. Chem. Phys., 11, 10705–10726, https://doi.org/10.5194/acp-11-10705-2011, 2011b.

Ryder, C. L., McQuaid, J. B., Flamant, C., Rosenberg, P. D., Washington, R., Brindley, H. E., Highwood, E. J., Marsham, J. H., Parker, D. J., Todd, M. C., Banks, J. R., Brooke, J. K., Engelstaedter, S., Estelles, V., Formenti, P., Garcia-Carreras, L., Kocha, C., Marenco, F., Sodemann, H., Allen, C. J. T., Bourdon, A., Bart, M., Cavazos-Guerra, C., Chevaillier, S., Crosier, J., Darbyshire, E., Dean, A. R., Dorsey, J. R., Kent, J., O'Sullivan, D., Schepanski, K., Szpek, K., Trembath, J., and Woolley, A.: Advances in understanding mineral dust and boundary layer processes over the Sahara from Fennec aircraft observations, Atmos. Chem. Phys., 15, 8479–8520, https://doi.org/10.5194/acp-15-8479-2015, 2015.
Tikhonov, A. N. and Arsenin, V. Y.: Solutions of Ill-Posed Problems, Math. Comput., 32, 1320–1322, 1978.

Tombette, M., Chazette, P., Sportisse, B., and Roustan, Y.: Simulation of aerosol optical properties over Europe with a 3-D size-resolved aerosol model: comparisons with AERONET

https://doi.org/10.5194/egusphere-2026-765
Preprint. Discussion started: 11 March 2026
© Author(s) 2026. CC BY 4.0 License.

data, Atmos. Chem. Phys., 8, 7115–7132, https://doi.org/10.5194/acp-8-7115-2008, 2008.

Wang, Y., Sartelet, K. N. N., Bocquet, M., and Chazette, P.: Assimilation of ground versus lidar observations for PM10 forecasting, Atmos. Chem. Phys., 13, 269–283, https://doi.org/10.5194/acp-13-269-2013, 2013.

Wang, Y., Sartelet, K. N. N., Bocquet, M., Chazette, P., Sicard, M., D'Amico, G., Léon, J. F. F., Alados-Arboledas, L., Amodeo, A., Augustin, P., Bach, J., Belegante, L., Binietoglou, I., Bush, X., Comerón, A., Delbarre, H., García-Vízcaino, D., Guerrero-Rascado, J. L. L., Hervo, M., Iarlori, M., Kokkalis, P., Lange, D., Molero, F., Montoux, N., Muñoz, A., Muñoz, C., Nicolae, D., Papayannis, A., Pappalardo, G., Preissler, J., Rizi, V., Rocadenbosch, F., Sellegri, K., Wagner, F., Dulac, F., Rizi, V., Rocadenbosch, F., Sellegri, K., Wagner, F., and Dulac, F.: Assimilation of lidar signals: application to aerosol forecasting in the western Mediterranean basin, Atmos. Chem. Phys., 14, 12031–12053, https://doi.org/10.5194/acp-14-12031-2014, 2014a.

Wang, Y., Sartelet, K. N. N., Bocquet, M., and Chazette, P.: Modelling and assimilation of lidar signals over Greater Paris during the MEGAPOLI summer campaign, Atmos. Chem. Phys., 14, 3511–3532, https://doi.org/10.5194/acp-14-3511-2014, 2014b.